Aggregation of solutes in bosonic versus fermionic quantum fluids

3	Alexandra J. Feinberg ¹ , Deepak Verma ^{1,2} , Sean M.O. O'Connell ^{1,3} , Swetha Erukala ¹ , Rico
4	Mayro P. Tanyag ^{1,4} , Weiwu Pang ⁵ , Catherine A. Saladrigas ^{6,7} , Benjamin W. Toulson ⁶ , Mario
5	Borgwardt ⁶ , Niranjan Shivaram ^{8,9} , Ming-Fu Lin ⁸ , Andre Al Haddad ¹⁰ , Wolfgang Jäger ¹¹ ,
6	Christoph Bostedt ^{10,12} , Peter Walter ⁸ , Oliver Gessner ^{6*} and Andrey F. Vilesov ^{1,13*}
7 8	¹ Department of Chemistry, University of Southern California, Los Angeles, California 90089, USA. ² RA3, Intel Corporation, Ronler Acres, 2501 NE Century Blvd, Hillsboro, OR 97124, USA.
9	³ Rosenstiel School of Marine and Atmospheric Sciences, 4600 Rickenbacker Cswy., Miami, FL, 33149, USA.
10	⁴ Department of Chemistry, Aarhus University, 8000 Aarhus C, Denmark.
11	⁵ Viterbi School of Engineering, University of Southern California, Los Angeles, California 90089, USA.
12	⁶ Chemical Sciences Division, Lawrence Berkeley National Laboratory, Berkeley, California 94720, USA.
13	⁷ Department of Chemistry, University of California, Berkeley, California 94720, USA.
14	⁸ SLAC National Accelerator Laboratory, 2575 Sand Hill Road, Menlo Park, California 94025, USA.
15	⁹ Department of Physics and Astronomy, Purdue University, West Lafayette, Indiana, 47907, USA.
16	¹⁰ Laboratory for Femotochemistry (LSF), Paul Scherrer Institut, Forschungsstrasse 111, 5232 Villigen-PSI,
17	Switzerland.
18	¹¹ Department of Chemistry, University of Alberta, Edmonton, Alberta T6G 2G2, Canada.
19	¹² LUXS Laboratory for Ultrafast X-ray Sciences, Institute for Chemical Sciences and Engineering, École
20	Polytechnique Fédérale de Lausanne (EPFL), CH-1015, Lausanne, Switzerland.
21	¹³ Department of Physics and Astronomy, University of Southern California, Los Angeles, California 90089, USA
22	*Corresponding authors

Abstract

Quantum fluid droplets made of helium-3 (³He) or helium-4 (⁴He) isotopes have long been considered as ideal cryogenic nanolabs, enabling unique ultracold chemistry and spectroscopy applications. The droplets were believed to provide a homogeneous environment in which dopant atoms and molecules could move and react almost as in free space, but at temperatures close to absolute zero. Here, we report ultrafast X-ray diffraction experiments on xenon-doped ³He and ⁴He nanodroplets, demonstrating that the unavoidable rotational excitation of isolated droplets leads to highly anisotropic and inhomogeneous interactions between the host matrix and enclosed dopants. Superfluid ⁴He droplets are laced with quantum vortices that trap the embedded particles, leading to the formation of filament-shaped clusters. In comparison, dopants in ³He droplets gather in diffuse, ring-shaped structures along the equator. The distorted shapes of droplets carrying both filaments and rings are direct evidence that rotational excitation is the root cause for the inhomogeneous dopant distributions.

Teaser

Clusters in ³He and ⁴He nanodroplets reveal dramatically different shapes showcasing the effect of superfluidity on aggregation.

Introduction

Quantum fluid nanodroplets made of liquid helium are exceptional hosts for isolated cryogenic matrix applications (1-5). The droplets readily pick up atoms and molecules (6), providing unique opportunities to study the formation of molecular complexes close to absolute zero temperatures. Indeed, the large degree of quantum mechanical delocalization in helium enables unique matrix configurations around the dopants, giving rise to a perfectly tailored void around each particular molecule (3).

Previously, small ⁴He droplets containing less than ~10⁴ atoms, roughly 10 nm in diameter, were used for the spectroscopic interrogation of molecules and molecular complexes at a temperature of about 0.4 K (1-5). It was long believed that, unlike immobilized dopant molecules in solid matrices, dopants in helium nanodroplets could move unhindered and stochastically (3, 7). Recent ultrafast X-ray coherent diffractive imaging (CDI) experiments with large xenon-doped superfluid ⁴He droplets, a few hundreds of nm in diameter, have revealed a dramatically different scenario (8-10). Instead of forming the once proposed ramified entities (7), dopant atoms were found to aggregate in arrays of elongated filament-shaped clusters (9, 10). This effect was assigned to inhomogeneities within the droplets due to the presence of quantum vortices, which attract dopant particles (11-14). The vortices were found to originate from an unavoidable rotational excitation of free helium droplets in the beam (8, 15-17), implying that the superfluid nature of ⁴He enhances the inhomogeneity of matrix-dopant interactions.

To provide unequivocal proof for the link between inhomogeneous dopant distributions, the superfluid nature of ${}^4\text{He}$ droplets, and their rotational excitation, comparative measurements are required on fermionic ${}^3\text{He}$ and superfluid, bosonic ${}^4\text{He}$ droplets. It is important to note that ${}^3\text{He}$ can also enter the superfluid state, but does so at much lower temperatures (T \sim 1 mK) (18, 19) than are present in our experiment (T \sim 0.15 K) (20). Thus, ${}^3\text{He}$ droplets act as a normal fluid under our experimental conditions and serve as a reference droplet devoid of vortices. Here, we present a comparative study of the aggregation of xenon atoms in sub micrometer sized ${}^3\text{He}$ and ${}^4\text{He}$ droplets. Our results show that, in fact, dopants are subject to a high degree of spatial confinement within both ${}^3\text{He}$ and ${}^4\text{He}$ nanodroplets, with each isotope giving rise to dramatically different dopant morphologies.

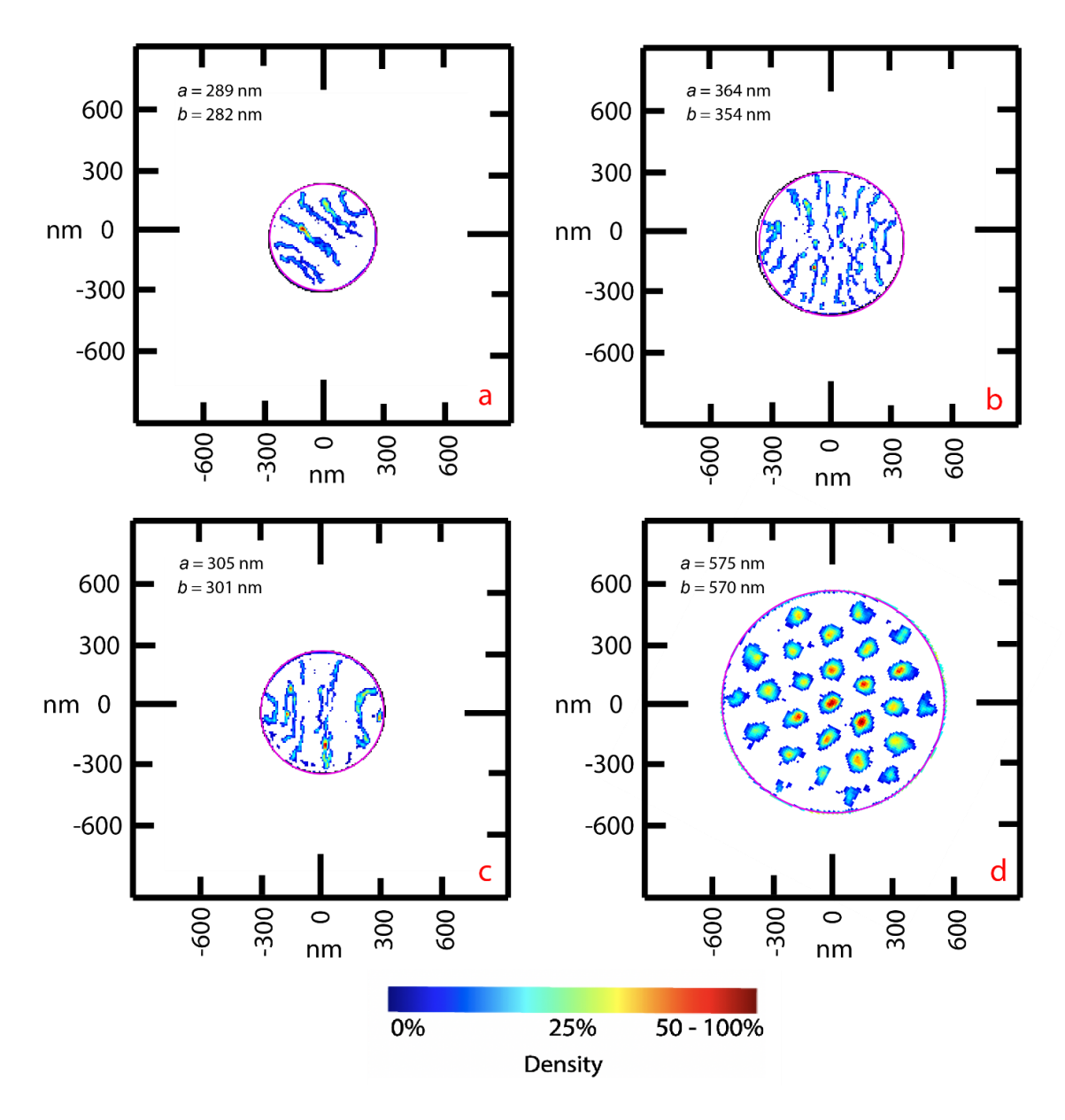


Fig. 1. Outlines (black) and xenon dopant density distributions (blue-red) of superfluid ⁴He droplets. Panels a-d show results for four different representative ⁴He droplets. The values *a* and *b* of the long and short half axis, respectively, of the droplet's projection onto the detector plane are given in each panel. For visualization, circular contours (magenta) have been superimposed on the droplets with a radius equal to that of the minor half axis. Closer inspection reveals slightly elliptical distortions, most prominent in droplet b.

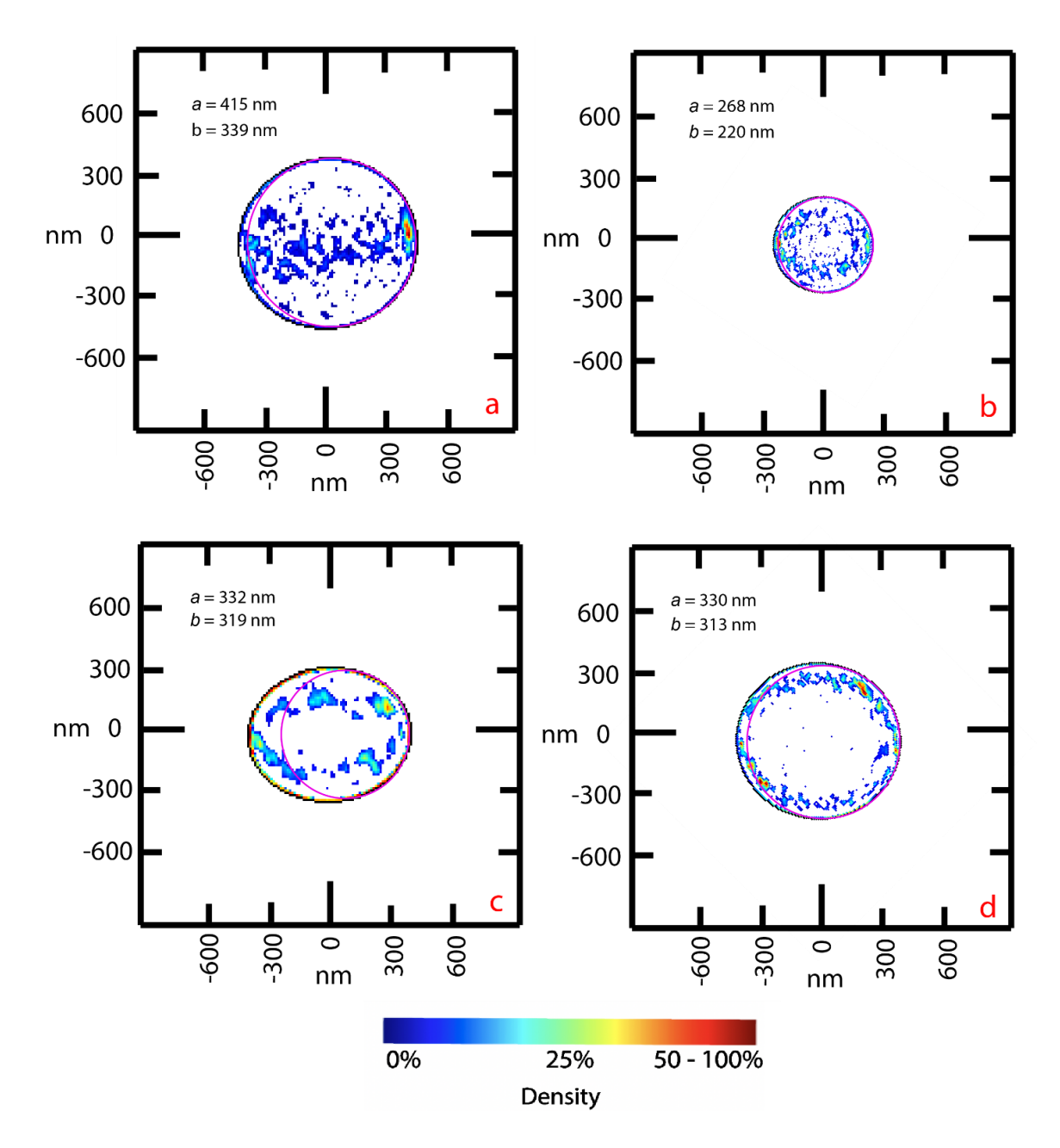


Fig. 2. Outlines (black) and Xe dopant density distributions (blue-red) of normal fluid ³He droplets. Panels a-d show results for four different representative ³He droplets. The values of the long and short half axis of the droplet's projection onto the detector plane are given in each panel. For visualization, circular contours (magenta) have been superimposed on the droplets with a radius equal to that of the minor half axis. Note the partly significant elliptical distortions of the droplet outlines.

Results

Figures 1 and 2 show plane projections of ⁴He and ³He droplets, respectively, with their reconstructed Xe dopant density distributions for a variety of representative droplets (10). The details on the reconstruction of density from diffraction images and the description of the results are described in the Materials and Methods (MM) section. The ³He and ⁴He droplets studied in this work have similar diameters in the range of 400-600 nm, containing on the order of 10⁹ helium atoms per droplet. Corresponding diffraction images are presented in the Supplementary Materials (SM).

Most outlines are ellipses, consistent with spheroidal, rotating droplets (8, 15, 17, 21, 22). In previous studies, it was found that a cryogenic fluid expansion into vacuum readily produces rotating ⁴He and ³He droplets (15, 17). It was also found that droplets of different isotopes have very similar average aspect ratios of about 1.05 for their projections on the detector plane (17). We hypothesized that during the passage of fluid helium through the nozzle, the fluid interacts with the nozzle channel walls and acquires vorticity, which is eventually transferred to the droplets. Figure 1 illustrates several ⁴He droplets and their dopant density distributions. As previously demonstrated (9, 10), the droplets contain several strongly aligned tracks of high density, which are assigned to xenon atoms aggregating inside the cores of quantum vortices. Vortices in Figs. 1a-c are viewed from the side, while vortices in Fig. 1d point toward the viewer, revealing their arrangement in a triangular lattice configuration that closely resembles the arrangements of vortices observed in rotating cylinders filled with ⁴He (11, 14) and in trapped Bose-Einstein condensates (23).

Results are dramatically different for xenon-doped 3 He droplets, as illustrated in Fig. 2. Here, xenon clusters either appear as a stripe (Fig. 2a) or as elliptical structures (Fig. 2b-d) that are aligned along the droplets' long axes. In Fig. 2d, xenon atoms form a loose ring of clusters on the droplet's periphery. During the imaging event, the X-ray beam forms an arbitrary angle with the droplet's figure axis; therefore, their real aspect ratios are larger than indicated by their outlines in Figs. 1 and 2, which correspond to projections of the droplets on the detector plane. The images are characterized by the two half axes of the droplet's projection, referred to as a and b (a > b), corresponding to a projection aspect ratio, AR = a/b. The formation of rings is observed in 3 He droplets having AR = 1.04 to AR = 1.2 (Fig. 2). A smaller amount of data was obtained for 4 He droplets during the same experimental run. Most of the intense, reconstructable 4 He images have a small aspect ratio (AR < 1.05). However, the results obtained during our previous studies show the formation of vortex arrays in droplets having up to AR = 2.4 (9). Thus, we observe confinement of dopants across a wide range of aspect ratios.

The lower boundaries for the droplet's angular velocity, estimated from their aspect ratios (17), are $\approx 1.1 \cdot 10^7$ rad/s and $\approx 1.5 \cdot 10^6$ rad/s for the droplets in Figs. 2c and 2d, respectively. In comparison, the angular velocity of the ⁴He droplet in Fig. 1d is estimated to be $\approx 1.7 \cdot 10^6$ rad/s based on the areal density of the vortices and using the Feynman relation (24). The pronounced alignment of the xenon cluster contours along the long axes of the ³He droplets strongly suggests that the xenon dopants form rings in the droplets' equatorial planes, with their apparent ellipticity determined by the viewing angle.

Statistically, there is a large difference between the shapes of the xenon density distributions within ³He and ⁴He droplets. No aligned filaments, which are characteristic for

superfluid ⁴He droplets, are observed in ³He droplets. Instead, these fermionic droplets contain diffuse ring-shaped structures. It is unlikely that the ring structures could be attributed to any impurities. The ³He gas used was 99.9% pure with the remaining 0.1% being mostly ⁴He.

Considering that ⁴He's solubility in ³He is ~0.1% at 0.15 K, any residual ⁴He will likely be dissolved in the ³He droplets. Even if any pockets of a ⁴He-rich phase were formed, they would be too small to give rise to any measurable effects in the diffraction patterns (*17*).

Discussion

It is immediately apparent from the dopant density distributions presented in Figs. 1 and 2 that helium nanodroplets are not homogenous nanolabs. In both isotopes, dopants are subject to unavoidable, high degrees of spatial confinement due to the droplets' rotation. In ⁴He, vortex-bound xenon is aligned along the minor axis of the droplets, as discussed in more detail elsewhere (9), whereas in ³He, xenon is confined along the droplet equator. The direct relation between the direction of the ³He droplet's long axis and the concentration of xenon along the equator is visually apparent in Fig. 2. The distorted shapes of ³He and ⁴He droplets carrying dopant rings and filaments, respectively, are direct evidence that rotational excitation is indeed the root cause for the inhomogeneous dopant distributions.

Clusters formed in fermionic ³He and bosonic ⁴He droplets exhibit distinctly different structures. Thus, nuclear spin, which has no impact on any property of ordinary solvents at higher temperatures, plays a crucial role in determining the aggregation dynamics of dopants at low temperatures. We propose that the mechanism for cluster formation in large helium droplets differs between superfluid ⁴He versus normal fluid ³He. In ⁴He, single xenon atoms are picked up

by the droplet, rapidly thermalize, and begin to move freely within the confines of the droplet's boundaries (3). Atoms form clusters upon collisions. At the same time, xenon atoms and small clusters are attracted to the cores of the vortices by hydrodynamic forces (11-14) and form large, filament-shaped aggregates. In comparison, in a ³He droplet devoid of vortices, xenon clusters will likely form throughout the entire droplet volume, followed by coalescence into larger globular cluster-cluster aggregates. However, due to the high viscosity of ³He droplets, dopants assume the same angular velocity as the host and congregate close to the droplet's surface along the equator, i.e., in a plane perpendicular to the direction of the angular momentum. The positions of the dopants are defined by a balance between centrifugal forces and the dopants' solvation potential (25). In principle, similar ring-shaped clusters are expected to be formed in classical rotating droplets (e.g., water droplets with heavy colloidal clusters), however we are unaware of such studies. The ring-shaped xenon structures appear to consist of separate, small (~50 nm) clusters, some of which exhibit branched shapes. The structures are likely defined during their formation and remain frozen at the low droplet temperature. The clusters appear to be separated and do not collapse into larger cluster-cluster aggregates, indicating that some mechanism stabilizes the porous network. Previously, it was proposed that some weakly interacting atoms (e.g., Magnesium) may form a so-called foam (26-28), where the atoms stay at sub-nm distance because of the shell of surrounding helium atoms. Whereas X-ray diffraction could be a useful technique for identifying the foam state, the resolution of the current smallangle soft X-ray scattering experiment of about 20 nm is insufficient to resolve spatial features on this level of detail. It is conceivable that the clusters have some interlinks that are too thin to be detected. The smallest compact cluster that can be detected in this work contains ~1000 xenon atoms and will appear in an image as approximately 3×3 pixels in size. This limit is set by the

149

150

151

152

153

154

155

156

157

158

159

160

161

162

163

164

165

166

167

168

169

170

threshold of the phase retrieval algorithm and the spatial resolution of the measurements (10). Future high-resolution experiments may shed more light on the atomic structure of aggregates obtained at temperatures close to 0 K.

The few 100-nm sized droplets in this study, which are produced from fragmentation of the supercritical fluid in the cryogenic nozzle, are marked by large angular velocities of 10⁶-10⁷ rad/s. This contrasts with the results for small droplets of few nm in diameter produced via aggregation of helium atoms. For example, extensive spectroscopy experiments on molecules in small (a few nm) ⁴He droplets did not indicate any presence of quantum vortices (*29*). On the other hand, centrifugal displacement of molecules from the droplet's center was discussed (*30*). The locations of molecules in small droplets could not be identified in the previous spectroscopy studies on either ³He or ⁴He, and the dopants are often assumed to reside close to the droplet's center (*3*, *4*). We observe that vortices in ⁴He are typically separated by distances of 100-200 nm, thus smaller droplets of 150 - 200 nm in diameter may contain just a single vortex. This shows that smaller ⁴He droplets between 50 - 100 nm in diameter may be devoid of vortices. Some other techniques of producing helium droplets at small velocity, other than in a molecular beam, may be considered to produce ⁴He droplets devoid of vortices.

Materials and Methods

Production and doping of ³He and ⁴He droplets:

Large nanodroplets are produced by expanding pressurized 4 He (99.9999%) or 3 He (99.9%) fluid through a cryogenic nozzle into vacuum with a stagnation pressure of $P_{0} = 20$ bar and a nozzle temperature $T_{0} = 5$ K (3, 8, 17, 31). At these expansion conditions, droplets with

average radii of ~160 nm and ~350 nm were produced for 3 He and 4 He, respectively (*17*). Once in vacuum, the droplets evaporatively cool to respective temperatures of 0.15 K for 3 He (*20*) and 0.38 K for 4 He (*32*). The droplets exit the source chamber with an average velocity of about 160 m/s for 3 He and 190 m/s for 4 He and subsequently enter the pickup chamber, which is filled with xenon (99.9%) gas. The droplets collide with, and pick up, several xenon atoms, evaporating off ~750 3 He or ~250 4 He atoms with the pickup of each xenon atom. The amount of xenon added is measured by monitoring the relative depletion of the mass M = 8 signal for 4 He (or M = 6 for 3 He), representative of He₂⁺ ions, in a quadrupole mass spectrometer installed in the terminal vacuum chamber (*8*). The droplets in Figs. 1 and 2 contain ~10⁹ helium atoms and between 10 5 - 10 6 xenon atoms. The 3 He gas was collected, purified and recirculated by a gas-recycling system as described elsewhere (*17*).

X-ray diffraction from Xe-doped ³He and ⁴He droplets:

Xenon-doped droplets are irradiated by a focused X-ray Free-Electron Laser (XFEL) beam operated at 1.5 keV (λ = 0.826 nm) (δ). The FEL beam consists of ultrashort X-ray pulses, containing up to ~10¹² photons/pulse, with a repetition rate of 120 Hz, a pulse energy of 1.5 mJ, and a pulse duration of ~100 fs (FWHM). The small pulse length and large number of photons per pulse enables the instantaneous capture of the shapes of individual droplets. Diffraction images are recorded with a pn-charge-coupled device (pnCCD) detector containing 1024 × 1024 pixels, each 75×75 μ m² in size, which is centered along the FEL beam axis ~735 mm downstream from the interaction point. The detector consists of two separate panels (1024 × 512 pixels each) located closely above and below the X-ray beam. Both panels have a central, rectangular cutout to accommodate the primary X-ray beam.

Density retrieval, size, and shape determination:

The diffraction patterns are recorded at small scattering angles and, thus, predominantly contain information on the column density of the droplets in the direction perpendicular to the detector plane. During the measurements, roughly 550 diffraction patterns from Xe doped ³He nanodroplets were obtained, whereas 200 patterns were obtained as a reference for Xe doped ⁴He droplets. Among them, only the brightest images containing more than ~10⁵ detected photons were selected for reconstruction (10). Ten brightest hits were selected from the ⁴He data, whereas 15 hits were selected from the ³He data. Using an iterative phase retrieval algorithm, termed Droplet Coherent Diffractive Imaging (DCDI), the density profiles of the Xe clusters inside the droplets are reconstructed and the sizes and shapes are determined (10). Similar ³He and ⁴He droplet reconstructions are compared based on size, aspect ratio, and overall number of photons detected.

Helium droplet shapes are described by the distances between the center and the surface in three mutually perpendicular directions: A > B > C. The observed diffraction patterns do not provide direct access to the actual values of A, B, and C, due to the droplets' unknown orientations with respect to the X-ray beam. Instead, the images are characterized by the two half axes of the projection of a droplet onto the detector plane, which are referred to as a and b (a > b), corresponding to a projection aspect ratio, AR = a/b. The majority (99%) of helium droplets are close to spherical with AR < 1.4 corresponding to oblate, axially symmetric shapes. For those shapes with AR < 1.4, the average aspect ratios for each isotope are similar, with $AR = 1.049 \pm 0.003$ for 3 He and 1.059 ± 0.005 for 4 He (17).

- M. Hartmann, R. E. Miller, J. P. Toennies, A. F. Vilesov, High-resolution molecular spectroscopy of van der Waals clusters in liquid helium droplets. *Science* 272, 1631-1634 (1996).
- 243 2. K. K. Lehmann, G. Scoles, Superfluid helium The ultimate spectroscopic matrix? *Science* **279**, 2065-2066 (1998).
- J. P. Toennies, A. F. Vilesov, Superfluid helium droplets: A uniquely cold nanomatrix for molecules and molecular complexes. *Angew. Chem. Int. Edit.* **43**, 2622 (2004).
- 4. M. Y. Choi *et al.*, Infrared spectroscopy of helium nanodroplets: novel methods for physics and chemistry. *Int. Revs. in Phys. Chem.* **25**, 15-75 (2006).
- 5. A. Mauracher *et al.*, Cold physics and chemistry: collisions, ionization and reactions inside helium nanodroplets close to zero K. *Phys. Reports* **751**, 1-90 (2018).
- M. Lewerenz, B. Schilling, J. P. Toennies, Successive capture and coagulation of atoms
 and molecules to small clusters in large liquid helium clusters. *J. Chem. Phys.* 102, 8191-8207 (1995).
- S. G. Alves, A. F. Vilesov, S. C. Ferreria Jr., Effects of the mean free path and relaxation in a model for the aggregation of particles in superfluid media. *J. Chem. Phys.* 130, 244506 (2009).
- 257 8. L. F. Gomez *et al.*, Shapes and vorticities of superfluid helium nanodroplets. *Science* **345**, 258 906-909 (2014).
- S. M. O. O'Connell *et al.*, Angular momentum in rotating superfluid droplets. *Phys. Rev. Lett.* 124, 215301 (2020).
- 261 10. R. M. P. Tanyag *et al.*, Communication: X-ray coherent diffractive imaging by immersion in nanodroplets. *Structural Dynamics* **2**, 051102 (2015).
- 11. G. Bewley, D. Lanthrop, K. Sreenivasan, Visualization of quantized vortices. *Nature* 441, 588 (2006).
- F. Coppens, F. Ancilotto, M. Barranco, N. Halberstat, M. Pi, Dynamics of impurity clustering in superfluid He4 nanodroplets. *Phys. Chem. Chem. Phys.* 31, 17423-17432 (2019).
- W. Guo, M. La Manita, D. Lathrop, S. Sciver, Visualization of two-fluid flows of superfluid helium-4. *PNAS* **111**, 4653-4658 (2014).
- E. J. Yarmchuck, M. V. J. Gordon, R. E. Packard, Observation of stationary vortex arrays in rotating superfluid-helium. *Phys. Rev. Lett.* 43, 214-217 (1979).
- B. Langbehn *et al.*, Three-dimensional shapes of spinning helium nanodroplets. *Phys. Rev. Lett.* 121, 255301 (2018).
- D. Rupp *et al.*, Coherent diffractive imaging of single helium nanodroplets with a high harmonic generation source. *Nat. Commun.* **8**, 493 (2017).
- D. Verma *et al.*, Shapes of rotating normal fluid He-3 versus superfluid He-4 droplets in molecular beams. *Phys. Rev. B* 102, 014504 (2020).
- 278 18. E. R. Dobbs, *Helium Three*. (Oxford University Press, New York, 2000).
- D. R. Tilley, J. Tilley, Superfluidity and Superconductivity. (Institute of Physics Publishing, Bristol, 1990).
- 281 20. B. G. Sartakov, J. P. Toennies, A. F. Vilesov, Infrared spectroscopy of carbonyl sulfide inside a pure 3He droplet. *J. Chem. Phys.* **136**, 134316 (2012).

- 283 21. F. Ancilotto, M. Barranco, M. Pi, Spinning superfluid He-4 nanodroplets. *Phys. Rev. B*284 97, 184515 (2018).
- 285 22. M. Pi, F. Ancilotto, M. Barranco, Rotating He-3 droplets. *J. Chem. Phys.* 152, 184111
 286 (2020).
- J. R. Abo-Shaeer, C. Raman, J. M. Vogels, W. Ketterle, Observation of vortex lattices in
 Bose-Einstein condensates. *Science* 292, 476 (2001).
- 289 24. R. P. Feynman, *Application of Quantum Mechanics to Liquid Helium*. (North Holland Publishing Company, Amsterdam, 1955), vol. 2, pp. 17-53.
- 291 25. C. Bernando, A. F. Vilesov, Kinematics of the doped quantum vortices in superfluid helium droplets. *J. Low. Temp. Phys.* **191**, 242-256 (2018).
- 293 26. E. B. Gordon, Impurity condensation in liquid and solid helium. *Low Temp. Phys.* **30**, 756-762 (2004).
- 27. S. Gode, R. Irsig, J. Tiggesbaumker, K. H. Meiwes-Broer, Time-resolved studies on the collapse of magnesium atom foam in helium nanodroplets. *New J. of Phys.* **15**, 015026 (2013).
- 298 28. J. Eloranta, Theoretical Study of Quantum Gel Formation in Superfluid He-4. *J. Low.* 299 *Temp. Phys.* 162, 718-723 (2011).
- 300 29. K. K. Lehmann, R. Schmied, Energetics and possible decay mechanisms of vortices in helium nanodroplets. *Phys. Rev. B* **68**, 224520 (2003).
- 30. K. K. Lehmann, Potential of a neutral impurity in a large helium droplet. *Molec. Phys.* 303 97, 645-666 (1999).
- 304 31. O. Bünermann *et al.*, Calcium atoms attached to mixed helium droplets: A probe for the 305 3He 4He interface. *Phys. Rev. B* **79**, 214511 (2009).
- 306 32. S. Grebenev, J. P. Toennies, A. F. Vilesov, Superfluidity within a small helium-4 cluster:
 307 The microscopic Andronikashvili experiment. *Science* 279, 2083-2086 (1998).
 308

Acknowledgements

- This material is based upon work supported by the National Science Foundation under
- 311 Grant No. DMR-1701077 and CHE-1664990 (A.F.V.). C.S., B.W.T., M.B. and O.G. are
- 312 supported by the U.S. Department of Energy, Office of Science, Office of Basic Energy
- 313 Sciences, Chemical Sciences, Geosciences and Biosciences Division, through Contract No. DE-
- 314 AC02-05CH11231. M.B. acknowledges support by the Alexander von Humboldt foundation.
- Portions of this research were carried out at the Linac Coherent Light Source (LCLS) at the
- 316 SLAC National Accelerator Laboratory. SLAC National Accelerator Laboratory, is supported by
- 317 the U.S. Department of Energy, Office of Science, Office of Basic Energy Sciences under

318 Contract No. DE-AC02-76SF00515. Additionally, we acknowledge the Natural Sciences and 319 Engineering Research Council of Canada. 320 321 **Author Contributions** 322 A.F.V., O.G. and C.B. conceived the experiment, A.J.F., D.V., S.M.O.O'C., S.E., C.A.S., 323 B.W.T., M.B., N.S., M.-F.L., P.W., O.G. and A.F.V. prepared and carried out the experiment. 324 A.J.F., D.V. and A.F.V. performed the data analysis. R.M.T. and W.P. contributed to the 325 development of the phase retrieval algorithm and took part in the preliminary experiments. 326 A.A.H. and C.B. provided support for online data analysis. S.M.O.O'C., W.J. and A.F.V. constructed the recycling apparatus for ³He gas. A.J.F., O.G. and A.F.V. wrote the manuscript. 327 328 329 **Competing Interests Statement** 330 The authors declare no competing financial interests. 331 **Data Availability Statement** 332 Raw data were generated at the Linac Coherent Light Source (LCLS) large-scale facility. 333 334 Derived data supporting the findings of this study are available from the corresponding author 335 upon request. 336

Supplementary Information (SI)

Diffraction Images

Figures S1a-d and S2a-d show the diffraction images for Xe-doped ⁴He and ³He droplets, respectively, from which the densities in Fig.1a-d and 2a-d of the main text were obtained. The images are plotted in the indicated logarithmic color scale and the patterns are cropped to the central 600×600 pixels of the 1024×1024 pixels detector. The diffraction images from ⁴He droplets in Fig. S1 exhibit circular ring structures close to the center and speckled patterns in the outer region due to scattering off the embedded Xe clusters. Figure S1d shows Bragg spots in a hexagonal arrangement, indicating that a highly ordered structure is contained inside the droplet. As with diffraction from ⁴He, the patterns from ³He droplets in Fig. S2 exhibit circular ring structures close to the center and speckled patterns in the outer region. However, in comparison to patterns from ⁴He droplets, the speckles are extended and seem to be arranged more closely along the rings. The different appearances of the diffraction patterns indicate different density distributions of Xe atoms inside ⁴He compared to ³He droplets, which are presented in Figs. 1 and 2, respectively, in the main text.

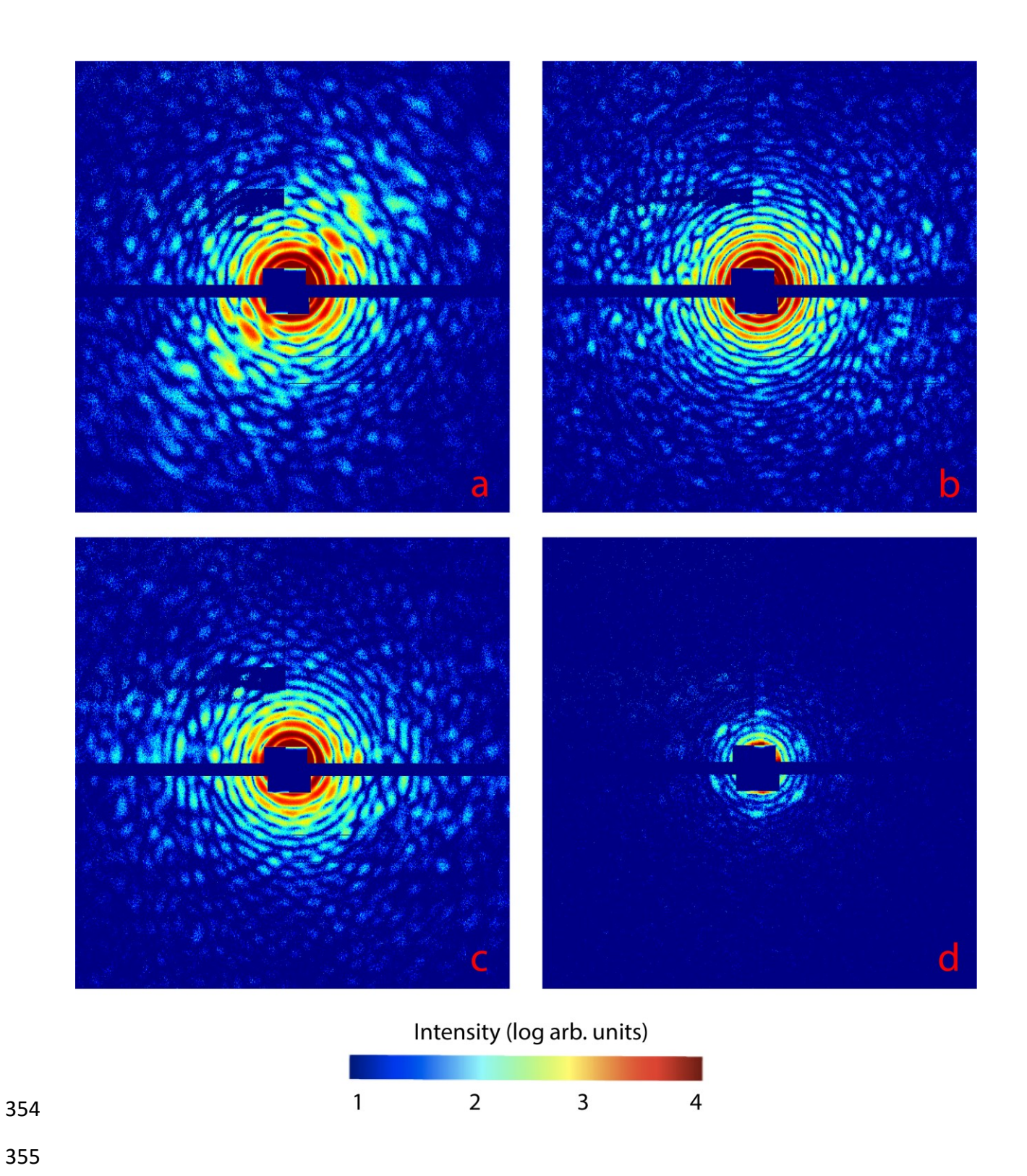


Figure S1. Diffraction images from ⁴He nanodroplets in a logarithmic color scale.

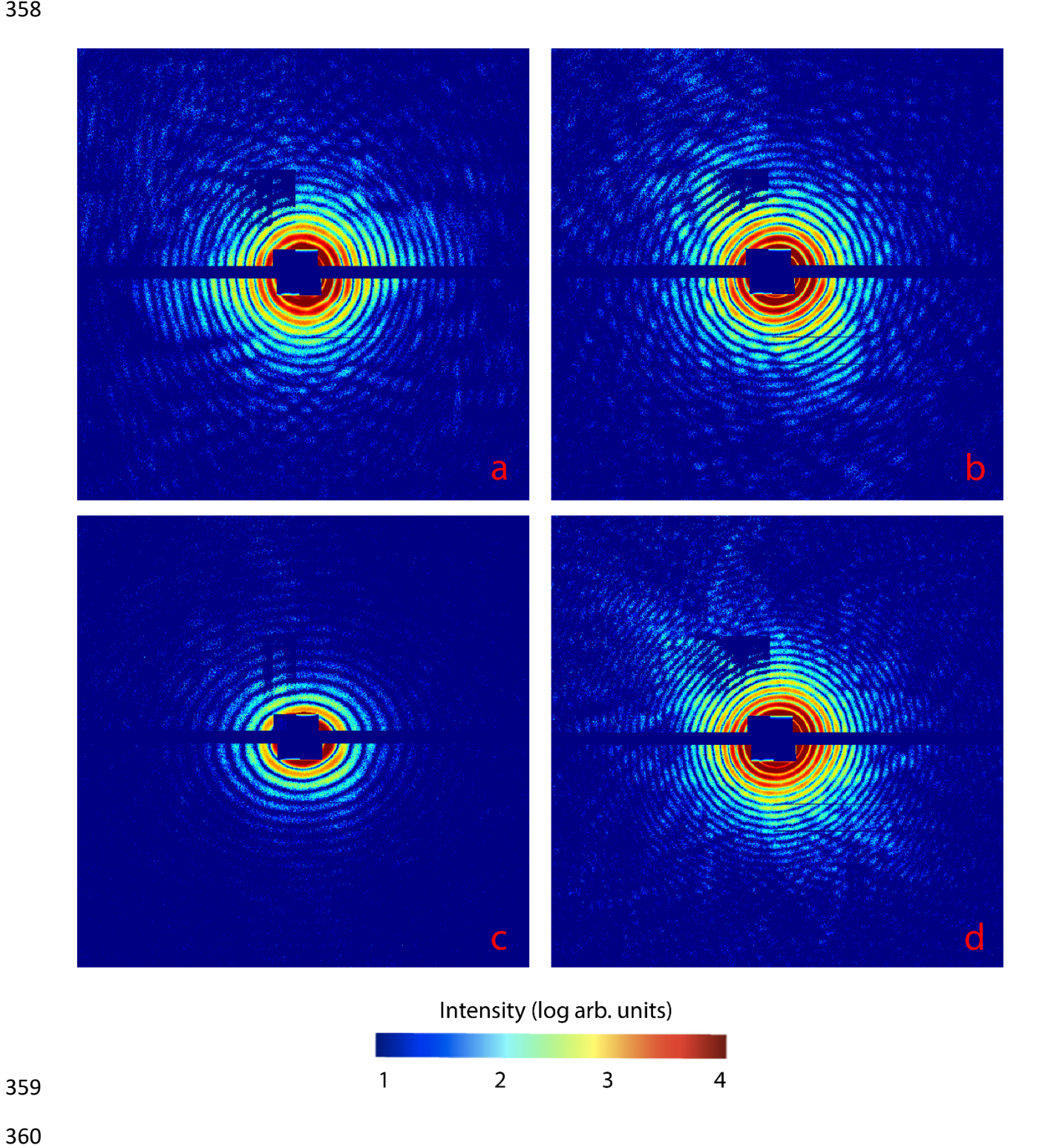


Figure S2. Diffraction images from ³He nanodroplets in a logarithmic color scale.